Two- and Three-Dimensional Effects in the Supersonic Mixing Layer

N. T. Clemens* and M. G. Mungal†
Stanford University, Stanford, California 94305

Experimental results are presented that compare the structure of the turbulent, planar mixing layer for three values of convective Mach number (0.28, 0.62, and 0.79), which span the range from low to moderate compressibility. Extensive planar laser Mie scattering visualizations are presented, where either mixed fluid or high-speed fluid is marked. The visualizations show that the supersonic mixing layer, when driven to low convective Mach number, behaves as an incompressible layer with characteristic two-dimensional, organized, Brown-Roshko structure. As convective Mach number increases, however, the mixing layer becomes highly three dimensional, with little apparent two-dimensional, large-scale organization. This change in structure is a compressibility effect and is not a Reynolds number effect.

Introduction

THE supersonic compressible mixing layer remains the object of intense experimental and theoretical study. Experimental studies to date have identified the convective Mach number[1,2] as an important parameter to quantify compressibility. Several studies have provided information on the growth rate,[2-7] large-scale structure,[7-9] turbulence properties,[4-6] and the effects of various perturbations to the flow.[10,11]

The structure, or topology, of the compressible layer remains an important issue in terms of its effect on entrainment and the subsequent mixing process. Although the turbulent structure has been addressed using the Toepler schlieren approach, the spatial integration of this method can easily mask three-dimensional flow physics. The present work involves observations of the turbulent structure using spatially resolved, planar approaches and is a continuation and extension of the work of Clemens et al.,[7] where alcohol droplet scattering visualizations for a convective Mach number of 0.6 were presented.

In addition to showing improved visualizations at a similar condition, visualizations at lower $(M_c = 0.28)$ and higher $(M_c = 0.79)$ levels of compressibility are presented. In Clemens et al.,[7] a droplet fog method is discussed where ethanol vapor that is seeded into the low-speed stream condenses as a result of mixing with the cold supersonic stream within the mixing layer. The fog, therefore, is a marker only of mixed fluid since neither pure high- nor low-speed fluid contains droplets; this method is analogous to marking the product that is formed as a result of a finite rate chemical reaction.[12,13] To check the accuracy of the visualizations obtained with this method, which could potentially be biased by nonuniform seeding or the finite rate of droplet formation, an additional independent visualization method is used in the present study. This second visualization technique uses the vapor screen method[14]; by seeding the high-speed side instead of the low-speed side, the ethanol vapor condenses within the supersonic nozzle, producing a fine fog that uniformly marks the high-speed fluid.

In the first method, since the fog is formed only within the mixing zones, it will be called the product formation method, in analogy with combustion systems. The second method is similar to the dilution of a passive scalar that has been extensively used in incompressible mixing layers, e.g., see Refs. 15 and 16, and, thus, will be called the passive scalar method. Both methods are described in detail in Clemens and Mungal.[17]

Experimental Setup

The facility is a supersonic mixing and combustion tunnel and has been previously described in Clemens et al.[7] It is of the blowdown type with typical run times of **30 s.** The wind tunnel, Fig. 1, is a two-stream mixing layer facility where the high-speed side is supersonic and the low-speed side is subsonic. The test section is 10 cm wide (z dimension) and 48 cm in length (x dimension). The height (y dimension) varies depending on the particular convective Mach number being studied. For the $M_c = 0.28$ case, the test section is 5.5 cm high, whereas for the higher compressibility cases, it is 7 cm high to accommodate the higher layer growth rates. The upper and lower test section guide walls are adjustable and allow for the setting of the streamwise pressure gradient.

The product formation and passive scalar visualizations to be shown later are obtained in similar ways, the only difference being the stream into which the seed is injected. Ethanol liquid is sprayed into the incoming flow using an atomizing spray nozzle that produces droplets <100 μm in diameter. The injection points are approximately 5 m upstream of the test section; the vapor laden flow passes through several elbows, two perforated plates, and one or two sections of honeycomb, thus becoming fully evaporated and uniformly mixed throughout the carrier fluid.

For the present studies, three different convective Mach numbers were achieved by varying the supersonic and subsonic Mach numbers and the low-speed gas molecular weight with the specific conditions given in Table 1. Three different nozzle blocks were used producing exit Mach numbers of 2.15, 1.97, and 1.5 for $M_c = 0.79$, 0.62, and 0.28, respectively. For the $M_c = 0.62$ and 0.79 cases, the test section lower wall was converged about 0.5 deg in order to obtain constant streamwise pressure. For the $M_c = 0.28$ case, however, both upper and lower walls were diverged about 0.5 deg in order to accelerate both flows to higher Mach numbers. For comparison, without accelerating the flow, the lowest convective Mach number attainable with the $M = 1.5$ nozzle is about 0.4. The
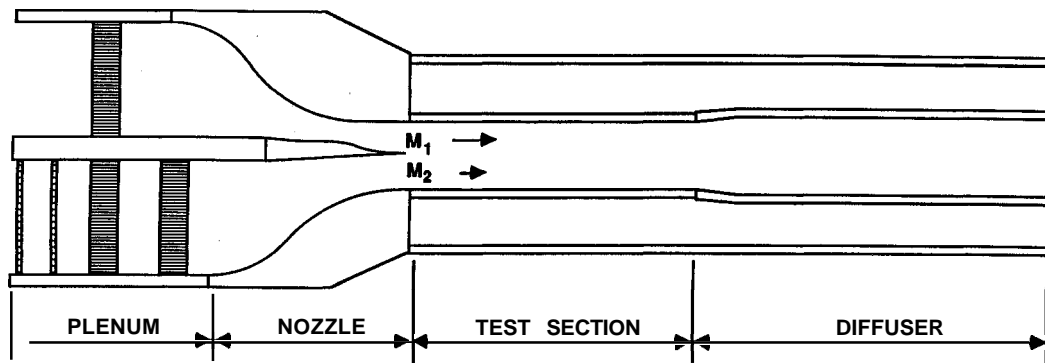
Fig. 1 Wind-tunnel schematic.

Table 1 Run conditions

	Case 1		Case 2		Case 3	
	Side 1	Side 2	Side 1	Side 2	Side 1	Side 2
Gas	Air	Air	Air	Air	Air	Argon
M	1.64	0.91	1.97	0.42	2.15	0.38
U, m/s	430	275	480	130	508	110
T_o, kPa	265	260	265	260	265	260
P_o, kPa	302	115	495	75	600	67
Flow rate, kg/s	1.6	0.77	1.8	0.37	1.84	0.39
Re, ($x = 45$ cm)	2×10^7	8×10^6	3×10^7	3×10^6	4×10^7	4×10^6
M_{C1}	0.28		0.62		0.79	
M_{C2}	0.28		0.62		0.73	
Density ratio	0.77		0.59		0.77	
Velocity ratio	0.63		0.28		0.22	
Re, ($x = 45$ cm)	2.3 x 105		8.0 x 105		1.0 x 10^6	
δ'_{pit}	0.036		0.061		0.063	
$\delta'_{pit}/(\delta'_{pit})_{inc}$	0.58		0.41		0.36	

$M_c = 0.79$ case is obtained by flowing an $M = 2.15$ airstream on an $M = 0.38$ argon stream.

For most of the runs, the average test section pressures were between 55 and 82 kPa, depending on the particular case. All gas total temperatures were about 270 K and decreased by about 10 K during a run. The Reynolds numbers based on velocity difference, local shear layer pitot thickness, and average kinematic viscosity of the two streams at the test section exit, $x = 45$ cm, were about 2.3 x 10^5, 8.0 x 10^5, and 1.0 x 10^6, for the low, medium, and high compressibility cases, respectively.

Diagnostics

The principal diagnostics used for this study are pitot probes, schlieren photography, and planar Mie scattering. The pitot probes are used to obtain an overall growth rate of the mixing layer, whereas the schlieren and Mie scattering images are used to obtain information on the large-scale structure.

Pitot Probes

The pitot tubes are constructed of 1.6-mm hypodermic needles of varying lengths, which are soldered to a 1.6-mm-thick x 2.54-cm-wide (in the streamwise direction) stainless steel strut. The flow, therefore, sees an obstruction that is only 1.6 mm wide and creates only a small perturbation on the flow. Earlier measurements using larger probes caused blockage effects to occur in the subsonic stream. The probe and strut were traversed vertically through the flow using a computer controlled stepping motor. Each pitot pressure trace consists of about 30 points and is completed in about 10 s.

Schlieren

For comparison with the Mie scattering images, Toepler schlieren images will also be presented. The schlieren system consists of a Xenon Nanolamp (20-ns pulse width), 30.5-cm-

diam F/6 parabolic mirrors, a razor blade knife edge, and a video camera (Pulnix TM540) as the imaging device.

Planar Mie Scattering

The planar Mie scattering images were obtained using a frequency doubled Nd:YAG laser (Quantel 660B) with a 6-ns pulse width, 150-mJ pulse energy, and a repetition rate of 10 Hz. The laser beam is formed into a sheet that is typically 15 cm wide and 250–300 μm thick at the waist. The detector is a standard CCD video camera (Pulnix TM540) whose video output is acquired using an IBM AT compatible computer with a Data Translation 2851 frame grabber. The images can be acquired and stored into 10 Mbytes of onboard computer memory at a rate of about 3 Hz. The present system accommodates a maximum of 80 images of 512 × 240 resolution. Even though single images are presented for brevity, they are selected to be representative of the general flow features for any given condition.

Clemens and Mungal[17] discuss both visualization methods in more detail, and they also address the issues of droplet coagulation and condensation uniformity. The following results are summarized from their discussion to which the reader is referred. Minimum perturbation to the flow is achieved for seeding levels corresponding to an alcohol mass fraction of 0.002 for the passive scalar method and 0.008 for the product formation method. The fog droplets in both cases have been measured to be <0.2 μm in diameter, with number densities >10^9/cm^3; however, it is more likely that they are about 0.05 μm in diameter with number densities of order 10^{11}/cm^3, consistent with the measurements of Clumpner.[18] Condensation times are believed to be about 50 μs based on the results of Wegener et al.[19] The uniformity of the scattering signal from the fog, for the passive scalar method, is found to be within 15–20% (after correcting for laser sheet nonuniformity and a slow increase in signal due possibly to coagulation) in all

directions across a 15-cm region. Evaporation of the droplets will occur for both methods when the fluid carrying the droplets becomes sufficiently diluted; complete evaporation will occur for dilution levels of about 5:1, which are expected to exist only at the small diffusion interface between the turbulent and nonturbulent fluid. The Stokes number, which is the ratio of the characteristic particle stop time[20] τ_p to an appropriate fluid mechanical time scale τ_f, is found to be 0.008 for a 0.2-μm alcohol droplet in air with a fluid mechanical time scale of $\delta/\Delta U$ (where δ is the shear layer visual thickness taken at $x = 15$ cm, and ΔU is the velocity difference across the layer). This value of Stokes number easily meets the requirements of Samimy and Lele[21] for correct flow visualizations whose numerical simulations suggest that the Stokes number, as defined earlier, should be less than about 0.25.

Results and Discussion

Mixing Layer Initial Conditions

Splitter plate boundary-layer measurements were not made but they are estimated using STAN7, a turbulent boundary-layer code.[22] The high-speed nozzle exit Reynolds numbers based on the distance from the throat, the nozzle exit velocity, and the freestream kinematic viscosity are 4.6 x 10^6, 7.5 x 10^6, and 9.0 x 10^6 for the $M_c = 0.28$, 0.62, and **0.79** cases, respectively. For Reynolds numbers of this magnitude, the boundary layers are expected to be turbulent; this was verified from close-up schlieren photographs. The calculated high-speed boundary-layer thicknesses δ_{99} at the nozzle exit are 1.6, 1.5, and 1.6 mm, whereas the momentum thicknesses are $\theta = 0.15$, 0.14, and 0.12 mm for the $M_c = 0.28$, 0.62, and 0.79 cases, respectively. The calculations of the boundary-layer thicknesses δ_{99} agree well with the thicknesses scaled from close-up schlieren photographs of about 1.5 mm. Therefore, for all of the planar visualizations presented later, x/θ varies from about 1000 to 2000 across the imaged region, whereas for the schlieren images, x/θ varies from 0 to 3000.

Figure 2 is a close-up schlieren image of the inlet flowfield for the $M_c = 0.28$ case, extending to about 3 cm downstream of the splitter tip. This region is seen to be quite complicated and suggests that the initial conditions are far from clean. The 1.5-mm-thick high-speed side boundary layer is seen to be turbulent. The splitter plate, which is 0.8 mm thick, appears thicker than the boundary layer because the collimated light beam is not perfectly parallel to the splitter plate. The schlieren image reveals a recirculation region immediately downstream of the tip, which causes an expansion fan to form on the high-speed side. The vortex shedding, which begins just downstream of the splitter tip, results from the shear layer formed between the high-speed stream and the recirculation region. The displacement effect of this local shear layer causes the flow to turn through a weak oblique shock, which combines with the fan in the far field. The vortices appear to disintegrate into fine scale turbulence after a few centimeters downstream of the tip.

The low-speed boundary layer is not visible due to the low Mach number of the low-speed stream; although there should also be a local shear layer on the low-speed side, it is not rendered visible due to the low compressibility of this side. It is interesting to note that, besides the larger scale shear layer vortices, this entire region downstream of the tip is composed of two different zones of very small-scale turbulence corresponding to regions that are dominated by either high- or low-speed fluid. It is from this initial condition that the flow structure, to be presented later, emerges.

Static Pressures

The test section static pressure distributions for the three cases are shown in Figs. 3. The pressure taps are located along the entire length of the test section on the top and bottom guide walls. For the $M_c = 0.28$ case, the pressures are seen to be matched at 12 psia, which corresponds to $M_1 = 1.5$ and
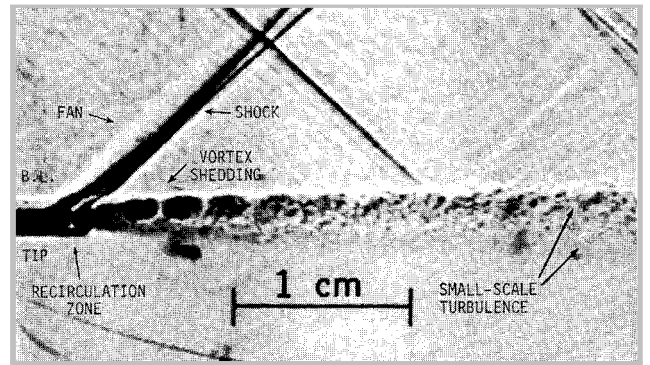

Fig. 2 Schlieren image of the first 3 cm downstream of the splitter tip (the knife edge is vertical and flow is from left to right).
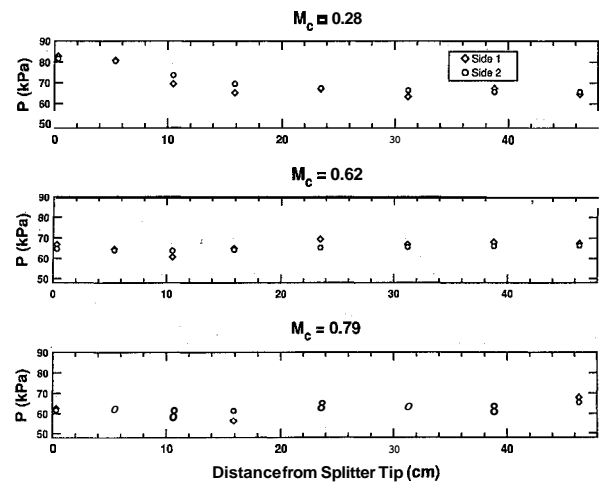

Fig. 3 Streamwise static pressure distributions: a) $M_c = 0.28$; b) $M_c = 0.62$; c) $M_c = 0.79$.

$M_2 = 0.7$. The two flows then quickly accelerate, reaching a constant pressure of about 9.5 psia from about 15–45 cm, which is our region of interest. The new freestream Mach numbers become 1.64 and 0.91 for the high- and low-speed streams, respectively. Figures 3 also show the static pressure distributions for the $M_c = 0.62$ and 0.79 cases. In both of these cases, the pressures are matched at the nozzle exits and vary <20% throughout the test section.

Growth Rates from Pitot Pressures

Pitot pressure traces were made at each convective Mach number at five axial stations extending from 7 to 40 cm downstream of the splitter tip. The $0.05\Delta P_{\text{pit}}$ and $0.95\Delta P_{\text{pit}}$ points (see Ref. 2) are used to define the edge of the layer, with the growth of the layer, in each case, found to be roughly linear throughout the downstream two-thirds of the test section. A linear best fit through all but the first pitot profile (i.e., from $x = 15$ to 40 cm) yields the growth rates, which, when normalized by the incompressible growth rate at the same velocity and density ratio,[2] are shown in Fig. 4. The uncertainties in the pitot measurement are due mainly to the small sample of points used in the fit, high-speed side pitot pressure nonuniformities of about 10% and run-to-run total pressure variations of about ±2%. For comparison, the pitot probe measurements of Papamoschou and Roshko[2] are also shown. The present results agree with their general trend toward decreasing growth rate with increasing convective Mach number.

The $M_c = 0.28$ point is sufficiently lower than that of Ref. 2, and so it requires some discussion. One possible reason is that the layer has not fully recovered from the induced pressure gradient in the upstream portion of the test section. This is not believed to be the case because Hermanson and Dimotakis[23] found subsonic mixing layers to immediately ad-

just to their freestream conditions. It is possible that in the present supersonic case there is a finite relaxation time that may be significant when compared to the short flow times. Shau and Dolling,[10] however, found the mixing layer to quickly adjust to a strong shock wave, regaining its unperturbed growth rate within about eight shear layer thicknesses downstream. Given that their Mach numbers were much higher than in the present study $(M_1 = 5, M_2 = 3)$, the present layer can be expected to relax in a shorter distance than this.

Other possible reasons for the reduced growth rate are as follows. Browand and Latigo,[24] Dziomba and Fiedler,[25] Mungal et al.,[26] and Bell and Mehta[27] have shown that the layer growth rate decreases by 25–30% if the high-speed boundary layer is tripped, all other things being equal. Of these, Refs, 24 and 25 show that the same growth rate is attained sufficiently far downstream, independent of the initial boundary-layer state. In addition, Goebel and Dutton[5] found that their supersonic mixing layers do not attain their fully developed state until the local Reynolds number, based on the velocity difference, the local thickness $(0.1\Delta U)$, and the average kinematic viscosity, exceeds 1×10^5. Accounting for the difference in their measure of local thickness and the pitot thickness used here, the Reynolds number for the $M_c = 0.28$ case meets their criterion at only the last two stations. Thus, the present case may not have reached its fully developed growth rate. Similar effects may have been present in the data in Ref. 2. Clearly, the related issues of the magnitude of the Reynolds numbers and the effect of the boundary-layer state (laminar vs turbulent) on the incompressible growth rate need to be resolved before a truly consistent normalization can be achieved.

Results for $M_c = 0.28$

Schlieren

A side-view schlieren image of the entire test section (0–45 cm, composite of three images) for the low compressibility case is shown in Fig. 5. For reference, the image of Fig. 2 is of the first 3 cm of this flowfield. Evident in Fig. 5 is the relatively weak shock that emanates from the splitter tip and another weak Mach wave that emanates from the supersonic nozzle/test section wall junction (also visible in Fig. 2). The schlieren photographs reveal large-scale organized Brown-
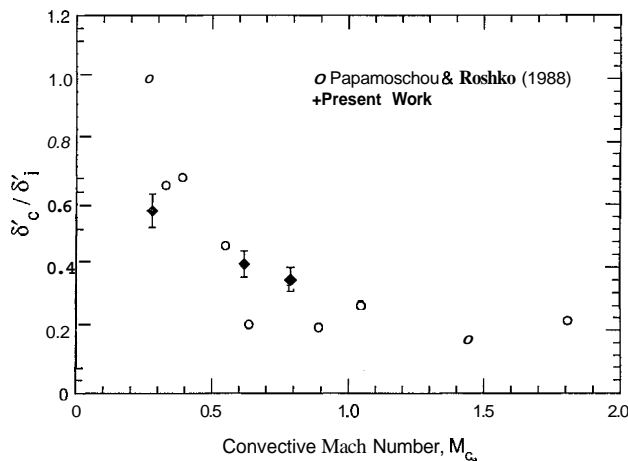
Roshko structures that appear at about 7 cm downstream and persist to the very end of the test section, where x/θ is about 3000 and $Re = 2.3 \times 10^5$. Thus, consistent with the results of Ref. 3, Brown-Roshko structures exist in very high Reynolds number, supersonic mixing layers, which are driven to the incompressible limit. Interestingly, the Brown-Roshko structures do not show signs of breaking up into three-dimensional turbulence with increasing streamwise distance. On the contrary, they usually appear the most robust near the exit station of the test section, as is seen in Fig. 5.

Additional schlieren images not shown here (but can be found in Ref. 28), at a convective Mach number of about 0.4, also show Brown-Roshko structures persisting to the exit station for a local Reynolds number almost three times higher than the $M_c = 0.28$ case. Positioning of the knife edge may explain why some researchers[2,5] did not find clear organized structures at low convective Mach number while others have.[3] In the present study, it was found that certain positions of the knife edge were optimal for visualizing the large-scale structures, whereas other positions highlighted only the small-scale turbulence.

Planar Mie Scattering Images

Three orthogonal planar cuts are made using the Mie scattering technique and are shown in Figs. 6–8. These three cuts are the side $(x\text{-}y)$, plan $(x\text{-}z)$, and end $(y\text{-}z)$ views. The end view is not strictly an end cut, as the camera was located at an angle of about 30 deg to the $x\text{-}y$ plane. All of the images shown, for all cases, were taken at the middle region of the test section from about $x = 15$–30 cm. Visualizations for the $M_c = 0.28$ and 0.62 cases were also taken at the $x = 30$–45-cm station (see Ref. 28) but are not presented here for brevity. It should be noted, however, that all conclusions
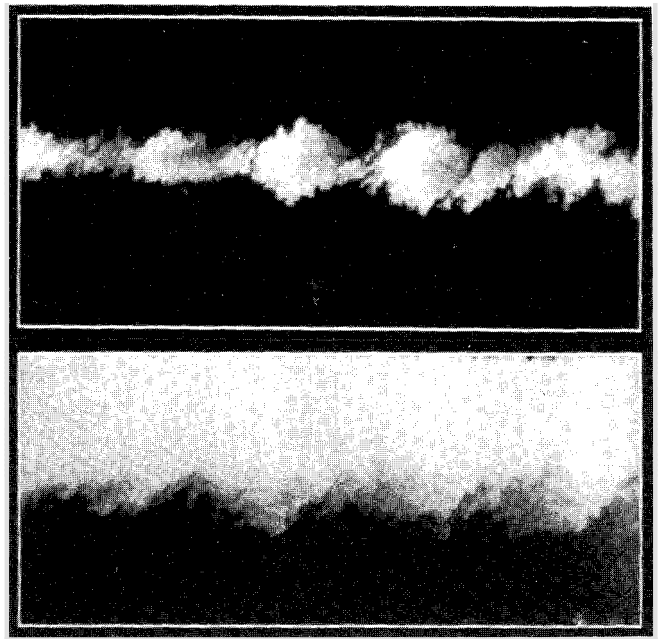

Fig. 6 Side-view Mie scattering for $M_c = 0.28$, $x = 15$–28 cm (flow is from left to right): a) (upper) product formation method; b) (lower) passive scalar method.

Fig. 4 Normalized growth rate vs convective Mach number.

Fig. 5 Composite schlieren for $M_c = 0.28$, $x = 0$–45 cm (flow is from left to right).

drawn from the upstream region also apply to locations farther downstream.

Figures 6 show planar side-view cuts using the product formation method (Fig. 6a) and the passive scalar method (Fig. 6b). Both images extend from 15–28 cm from the splitter tip and reveal, unambiguously, the organized structures that are seen in the schlieren images, but with much greater detail. In both images, large coherent vortex cores separated by thinner braid regions can be seen. The product formation method is seen to be superior in visualizing the details of the mixing layer due to its natural contrast on both the high- and low-speed side interfaces. In Fig. 6b, the limited dynamic range makes it difficult to distinguish the high-speed side interface. By examining the bottom interfaces, however, the underlying structure of both images is seen to be similar. As a general

Fig. 7 Plan-view Mie scattering for $M_c = 0.28$, $x = 15$–30 cm (flow is from left to right): a) (upper) product formation method; b) (lower) passive scalar method.

rule, the product formation method will highlight turbulent motions that bring mixed fluid next to unmixed fluid, whereas the passive scalar method will highlight motions that bring pure high-speed fluid next to pure low-speed fluid. The proper way to compare the two images is to mark only the gray scales of Fig. 6b since these correspond to mixed fluid. Additional details seen in Figs. 6 are smaller scale structures that reside on the larger scales in addition to variations of concentration within the vortex cores.

The large-scale fluid mechanical time scale in the $M_c = 0.28$ case, approximated to be $\delta/\Delta U = 25$ μs at $x = 15$ cm (which is also the inverse of the large-scale strain rate), is shorter than the measured condensation time.[''] Fluid that feels these large-scale strain rates, therefore, should not have time to form and should not be visualized. Figure 6a, however, shows that the product has formed within the highly strained braid regions between the large-scale structures. This implies that either the condensation time is actually shorter than was measured by Wegener et al.[19] or that the braid time scales are longer than $\delta/\Delta U$. The latter view is supported by the observation that the braids are relatively fat, suggesting that there is some amount of local mixing that could increase the residence time for braid fluid. Although braid fluid is usually visible, sometimes the scattering intensities are clearly lower than in the core regions (see, e.g., Figs. 8); it appears, then, that braid strain rates are high enough for some finite rate effects to be seen.

In order to establish if the structures seen in the side views are two dimensional and span the mixing layer, plan-view cuts through approximately the middle of the layer (in the y direction) are shown in Figs. 7 using both visualization methods. These images extend from 15–30 cm from the splitter tip and span the central 5 cm (out of a width of 10 cm) of the test section; thus, the side-wall boundary layers are not in the field of view. For both visualization methods, the structures are seen to span the width of the layer, in agreement with previous studies in incompressible flows.[16,29] It should be noted that the signals in Figs. 7a and 7b are not equivalent since, in Fig. 7a, the cores are marked, whereas in Fig. 7b, high-speed fluid
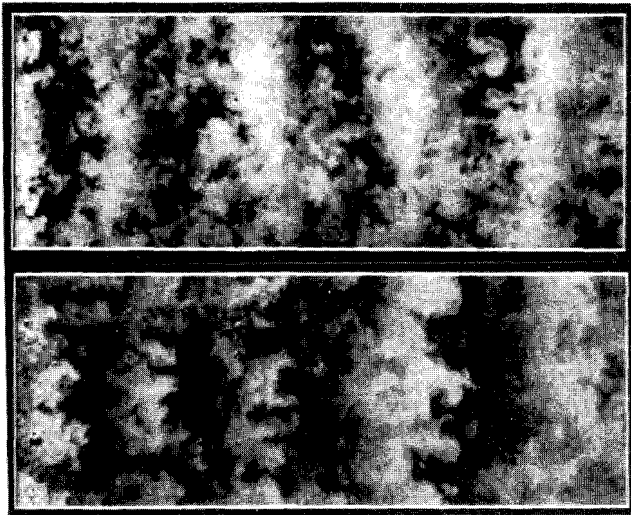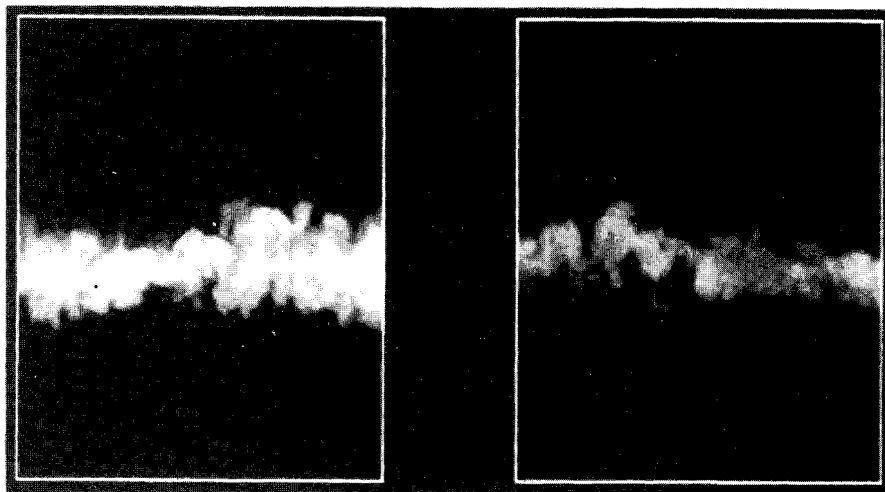

Fig. 8 Product formation end-view Mie scattering images for $M_c = 0.28$, $x = 18$ cm: a) (left) cut through vortex core; b) (right) cut through braid.
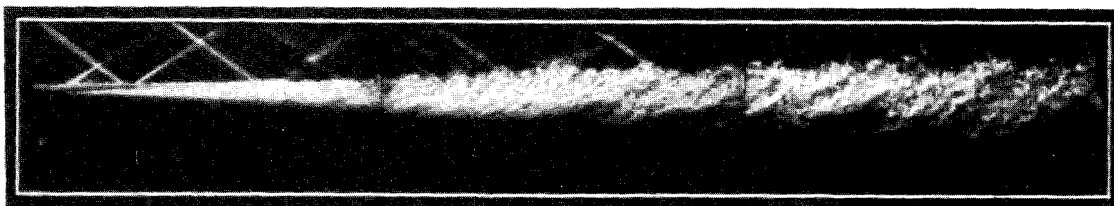

Fig. 9 Composite schlieren for $M_c = 0.62$, $x = 0$–45 cm (flow is from left to right).

between the cores are marked. Also apparent in Figs. **7** are the secondary streamwise braid vortices that are present in low-speed incompressible mixing layers.[29] The braid structures are especially apparent in the passive scalar images since the braid regions are thin and tend to bring high- and low-speed fluid into close proximity.

In Figs. **8**, end-view cuts using only the product formation method are shown; Fig. 8a shows a cut through what appears to be a core of a large-scale structure, whereas in Fig. 8b, a braid cut is shown. The core is seen to be relatively large and homogeneous when compared to the braid structure, which is thinner and highly convoluted, as is expected from incompressible results.[29]

Results for $M_c = 0.62$

Schlieren

Side-view schlieren images are shown in Fig. 9 for the $M_c = 0.62$ case. Again, two weak shock waves are seen near the nozzle exits. The large-scale organized structures clearly seen in the low compressibility case are apparently no longer present. In fact, it is surprising how little structure can be seen as compared to Fig. 5.

Planar Mie Scattering

Figures 10 show side-view cuts for the $M_c = 0.62$ case, covering 15–28 cm from the splitter tip. The product formation method is shown in Fig. 10a and shows structures that appear different from those of Figs. 6, as they do not appear as distinctly roller-like and are not as regularly spaced. Sometimes distinct rollers are seen but they are rarely preceded or followed by other distinct rollers. The passive scalar images, Fig. 10b, also show this decrease in regularity. A more subtle difference between these images and those of Figs. 6 is that the high- and low-speed interfaces appear more jagged, with freestream fluid making sharp intrusions into the layer.

Even though the structures in the side views appear less organized, only plan views will reveal if they are two dimensional. Figures 11 show plan-view cuts through the middle of the layer for both methods, extending from 15–30 cm from the splitter tip. Neither image reveals structures that are highly two dimensional since only occasionally do structures appear that span the width of the layer. Not only do the plan views appear three dimensional, but they appear to be lacking any spatial regularity at all. There seems to be little indication as to the directionality of the flow, except for a possible increase in the number of dark streamwise streaks.

End-view cuts taken at 22 cm from the splitter tip, using only the product formation method, are shown in Figs. 12. Although these images do not appear to be greatly different from the $M_c = 0.28$ case, there are some subtle differences. First, the end views do not exhibit the large core vs thin highly convoluted braid structure, as **is** found in the low compressibility case. Instead, the end views appear as highly convoluted structures of similar size. This is consistent with the observation that spanwise bands of mixed and unmixed fluid are not present in the plan views since a long thin region in the end view would appear as a spanwise band in the plan view. A second difference is that often small jets of mixed fluid are ejected from the layer,-as can be seen in Fig. 12a (and in Fig. 10a on the low-speed side of the layer). These ejections may be mushroom structures caused by small-scale counter-rotating vortices.

The differences just discussed between the $M_c = 0.28$ and 0.62 cases are not due to a Reynolds number effect but to a compressibility effect. This is easily shown by considering the structure of the $M_c = 0.28$ case at $x = 45$ cm vs the structure of the $M_c = 0.62$ case near the 15-cm station. For this situation, the Reynolds numbers are nearly matched since, in the first case, $Re, = 2.3 \times 10^5$, whereas for the second case, $Re, = 2.8 \times 10^5$. Even with equal Reynolds numbers, how-
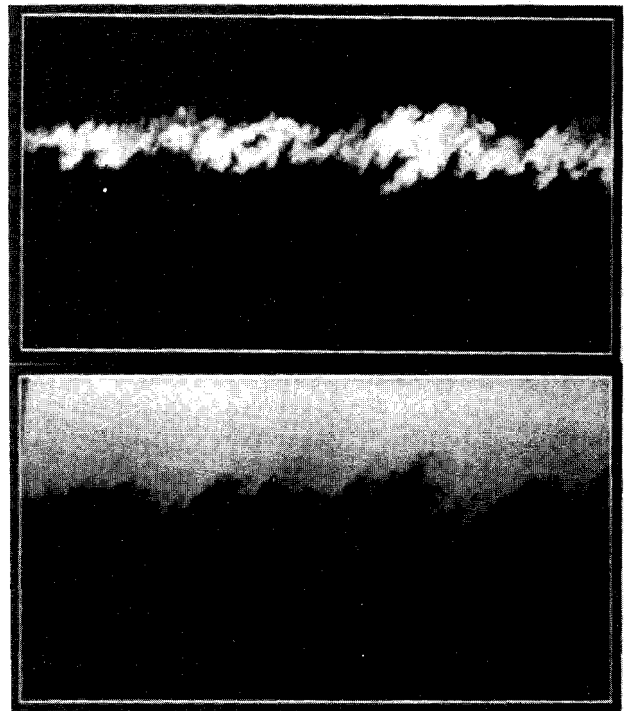

Fig. 10 Side-view Mie scattering for $M_c = 0.62$, $x = 15$–28 cm (flow is from left to right): a) (upper) product formation method; b) (Lower) passive scalar method.
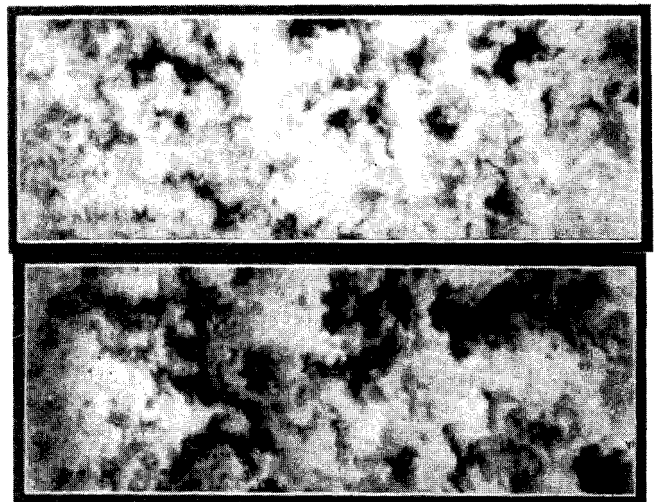

Fig. 11 Plan-view Mie scattering for $M_c = 0.62$, $x = 15$–30 cm (flow is from left to right): a) (upper) product formation method; b) (lower) passive scalar method.

ever, the structure is not the same for the two cases. Furthermore, as mentioned earlier, for an $M_c = 0.4$ case not shown, Brown-Roshko structures persisted for Reynolds numbers over twice as high as that for the $M_c = 0.62$ case at the 15-cm location.

Results for $M_c = 0.79$

Schlieren

Figure 13 shows a side-view schlieren composite of the entire test section for the $M_c = 0.79$ case. As in the preceding case, large-scale structures are not readily apparent, although the planar cuts do reveal large-scale, albeit, three-dimensional, structures. This suggests that the spatial integration of the schlieren technique averages out the effects of the large-scale structures.
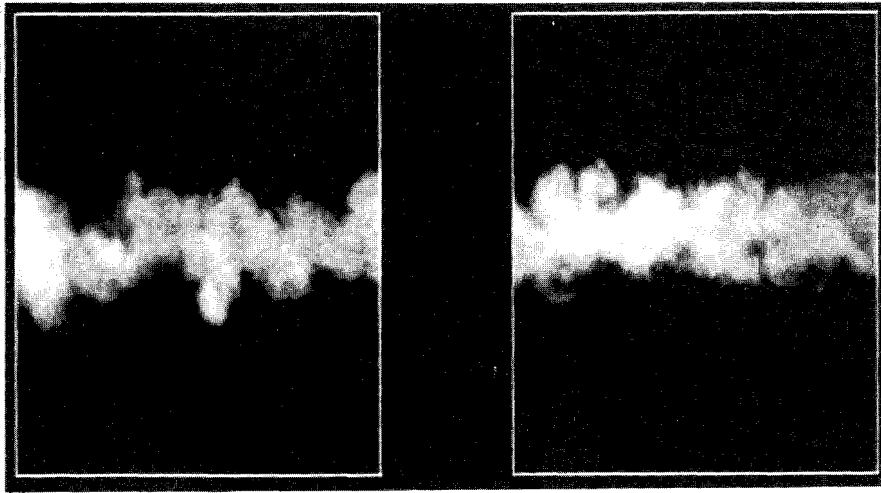
Fig. **12** Product formation end-view Mie scattering images for $M_c = 0.62$, $x = 22$ cm.

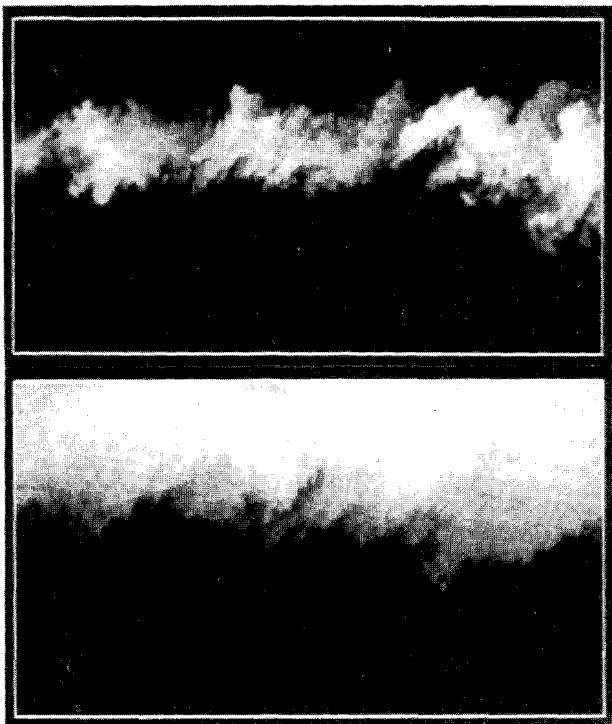Fig. **13** Composite schlieren for $M_c = 0.79$, $x = 0-45$ cm (flow is from left to right).

Fig. **14** Side-view Mie scattering for $M_c = 0.79$, $x = 18-33$ cm (flow is from left to right): a) (upper) product formation method; b) (lower) passive scalar method.

Planar Mie Scattering

Side-view images using both visualization methods are shown in Figs. 14. Although their structure looks similar to the $M_c = 0.62$ case, they appear larger because the imaged region is farther downstream, from $x = 18-33$ cm. By examining a large number of side views (approximately 80 for each case),
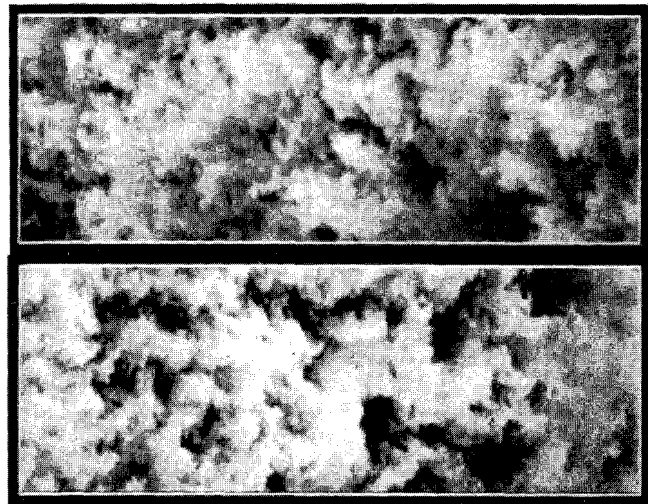

Fig. **15** Plan-view Mie scattering for $M_c = 0.79$, $x = 18-33$ cm (flow is from left to right): a) (upper) product formation method; b) (lower) passive scalar method.

there appears to be no obvious differences between the $M_c = 0.79$ and 0.62 cases.

Plan views, shown in Figs. 15, similarly show the highly three-dimensional structure of the medium compressibility case. Although both methods reveal three-dimensional structure, there is a subtle difference. The passive scalar images, for both the $M_c = 0.62$ and 0.79 cases, exhibit a greater number of dark streamwise streaks as compared to the product formation method. These streaks are different than the ones seen in Figs. 7 since they are not associated with two-dimensional rollers and appear on a larger scale. Since the passive scalar method marks high-speed fluid, these dark streaks represent pure low-speed fluid, which is probably carried to the center of the layer by streamwise vortices. The fact that
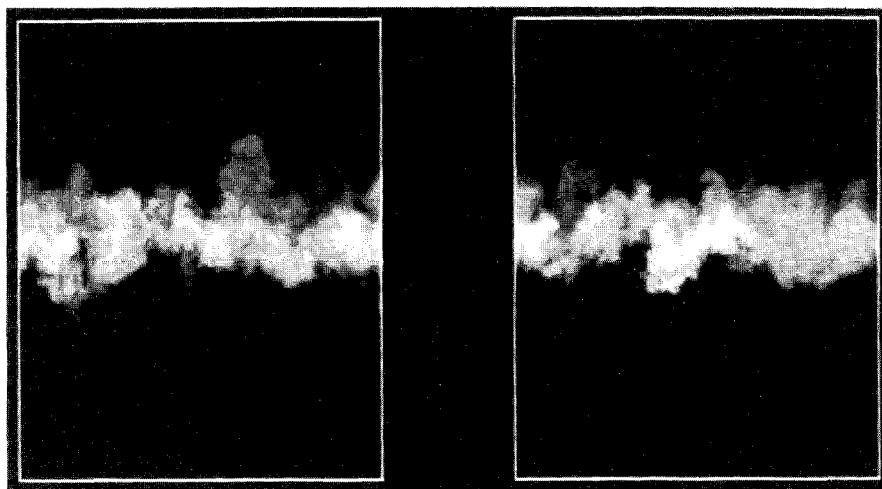
Fig. 16   Product formation end-view Mie scattering images for $M_c = 0.79$, $x = 23$ cm.

the streaks are not as apparent with the product formation method suggests that high-speed fluid is not entrained in a predominantly streamwise manner. This is because in the product formation method, both pure low- and high-speed fluids appear dark; thus, the high-speed fluid must be entrained such that the low-speed streaks are disrupted. This would be the case if high-speed fluid is entrained through both streamwise and spanwise motions. Additional evidence for this is found in Ref. 7, where it was found that cuts through the low-speed side of the layer revealed considerably more streamwise structure than similar cuts through the middle of the layer, and cuts through the high-speed side revealed spotty regions of mixed fluid.

End views at *23* cm from the splitter tip for the high compressibility case are shown in Figs. 16. Again, these images exhibit a structure similar to $M_c = 0.62$ case, as can be seen by comparing to Figs. 12. The end-view structures are highly convoluted and exhibit similar ejections of fluid into the free-streams.

Taken as a whole, these images for all three cases reveal a mixing layer structure that makes a transition from two-dimensional behavior at low levels of compressibility to three dimensionality at higher levels of compressibility. Additional images taken at a convective Mach number of 0.5 show true transitional behavior, where both two-dimensional rollers and irregular, three-dimensional structures are present at different instants. It is not clear, however, if as compressibility increases further a new organized structure would exist, as is suggested by the direct numerical simulations of Sandham and Reynold~, where a hairpin-type structure is found to exist at a convective Mach number of about *0.8.* The present visualizations at $M_c = 0.79$, however, look much less structured than the simulation results; it may be difficult to compare both sets of results since, in Ref. 30, low pressure contours are shown that mark vortex cores, whereas in the present work, scalars are imaged that do not directly mark vortical regions. Even so, there is agreement in the sense that there is an increase in both three dimensionality and streamwise structure. We note that, consistent with the present results, the sonic eddy model of Breidenthal[31] also predicts an increase in three dimensionality, with increasing compressibility.

Conclusions

The structure of the supersonic mixing layer is found to be highly dependent on the value of the convective Mach number. For $M_c = 0.28$, the turbulent structure is found to be relatively two dimensional, with Brown-Roshko structures persisting to several thousand x/θ and local Reynolds numbers of over 2×10^5. The secondary streamwise braid structure is also clearly evident. For $M_c = 0.62$ and 0.79, the structure

is highly three dimensional and seldom shows signs of two dimensionality. The large scales do not appear to be organized at all, except for a possible increase in streamwise organization near the low-speed edge of the layer. These effects are due to compressibility and are not due to differing Reynolds numbers. These results are important since the more three-dimensional large-scale structure may lead to values of the entrainment ratio and mixed fluid concentrations that are significantly different from the incompressible case. Three dimensionality may also impact one's ability to force and control compressible mixing layers. Finally, it is noted that, in order to achieve a proper compressible growth rate normalization curve, the state of the incoming boundary layers (laminar vs turbulent) and the achievement of an asymptotic growth rate are issues that deserve further attention.

References

[1]Bogdanoff, D. W., "Compressibility Effects in Turbulent Shear Layers," *AZAA Journal,* Vol. 21, No. 6, 1983, pp. 926, 927.

[2]Papamoschou, D., and Roshko, A., "The Compressible Turbulent Shear Layer: An Experimental Study," *Journal of Fluid Mechanics,* Vol. 197, 1988, pp. 453–477.

[3]Chinzei, N., Masuya, G., Domuro, T., Murakami, A., and Kudou, K., "Spreading of Two-Stream Supersonic Mixing Layers," *Physics of Fluids,* Vol. 29, No. 5, 1986, pp. 1345–1347.

[4]Elliot, G., and Samimy, M., "Compressibility Effects in Free Shear Layers," AIAA Paper 90-0705, Jan. 1990.

[5]Goebel, S. G., and Dutton, J. C., "Velocity Measurements of Compressible, Turbulent Mixing Layers," *AIAA* Paper 90-0709, Jan. 1990.

[6]Ikawa, H., and Kubota, T., "Investigation of Supersonic Turbulent Mixing Layer with Zero Pressure Gradient," *AIAA Journal,* Vol. 13, No. 5, 1975, pp. 566–572.

[7]Clemens, N. T., Mungal, M. G., Berger, T. E., and Vandsburger, U., "Visualizations of the Structure of the Turbulent Mixing Layer Under Compressible Conditions," *AIAA* Paper 90-500, Jan. 1990.

[8]Papamoschou, D., "Structure of the Compressible Turbulent Shear Layer," AIAA Paper 89-0126, Jan. 1989.

[9]Fourguette, D. C., Mungal, M. G., and Dibble, R. W., "Time Evolution of the Shear Layer of a Supersonic Axisymmetric Jet," *AZAA Journal,* Vol. 29, No. 7, 1991, pp. 1123–1130.

[10]Shau, **Y.** R., and Dolling, D. **S.**, "Experimental Study of Spreading Rate Enhancement of High Mach Number Turbulent Shear Layers," AIAA Paper 89-2458, July 1989.

[11]Samimy, M., Erwin, D. W., and Elliot, G. S., "Compressibility and Shock Wave Interaction Effects on Free Shear Layers," AIAA Paper 89-2460, July 1989.

[12]Mungal, M. G., and Frieler, C. E., "The Effects of Damkohler Number in a Turbulent Shear Layer," *Combustion and Flame,* **Vol.** 71, 1988, **pp. 23, 24.**

[13]Broadwell, J. E., and Mungal, M. G., "Molecular Mixing and Chemical Reactions in Turbulent Shear Layers," *22nd International Symposium on Combustion,* Combustion Inst., Pittsburgh, PA, 1988, pp. 579–587.

[14]McGregor, I., "The Vapor Screen Method of Flow Visualization," *Journal of Fluid Mechanics,* Vol. 11, No. 4, 1961, pp. 481–511.

[15]Batt, R. G., "Turbulent Mixing of Passive and Chemically Reacting Species in a Low Speed Shear Layer," *Journal of Fluid Mechanics,* Vol. 82, 1977, pp. 53–95.

[16]Breidenthal, R. **E.,** "Structure in Turbulent Mixing Layers and Wakes Using a Chemical Reaction," *Journal of Fluid Mechanics,* Vol. 109, 1981, pp. 1–24.

[17]Clemens, N. T., and Mungal, M. G., "A Planar Laser Mie Scattering Technique for Visualizing Supersonic Mixing Flows," *Experiments in Fluids,* Vol. 11, No. 2/3, 1991, pp. 175–185.

[18]Clumpner, J. A., "Light Scattering from Ethyl Alcohol Droplets Formed by Homogeneous Nucleation," *Journal of Chemical Physics,* Vol. 55, 1972, pp. 5042–5045.

[19]Wegener, P. **P.,** Clumpner, J. **A.,** and Wu, B. J. C., "Homogeneous Nucleation and Growth of Ethanol Drops in Supersonic Flow," *Physics of Fluids,* Vol. 15, No. 11, 1972, pp. 1869–1876.

[20]Melling, A., "Seeding Gas Flows for Laser Anemometry," AGARD-CP-399, 1986, pp. 8.1–8.11.

[21]Samimy, M., and Lele, S. K., "Motion of Particles with Inertia in a Compressible Free Shear Layer," *Physics of Fluids* **A** (to be published); "Particle-Laden Compressible Free Shear Layers," AIAA Paper 90-1977, July 1990.

[22]Crawford, M. E., and Kays, W. M., "STAN5—A Program for Numerical Computation of Two-Dimensional Internal and External Boundary Layer Flows," NASA CR-2742, Dec. 1976.

[23]Hermanson, J. C., and Dimotakis, P. E., "Effects of Heat Release in a Turbulent, Reacting Shear Layer," *Journal of Fluid Mechanics,* Vol. 199, 1989, pp. 333–375.

[24]Browand, F. K., and Latigo, B. O., "Growth of the Two-Dimensional Mixing Layer from a Turbulent and Nonturbulent Boundary Layer," *Physics of Fluids*, Vol. 22, No. 6, 1979, pp. 1011–1019.

[25]Dziomba, B., and Fiedler, **H.** E., "Effect of Initial Conditions on Two-Dimensional Free Shear Layers," *Journal of Fluid Mechanics,* Vol. 152, 1985, pp. 419–442.

[26]Mungal, M. G., Hermanson, J. C., and Dimotakis, P. **E.,** "Reynolds Number Effects on Mixing and Combustion in a Reacting Shear Layer," *AIAA Journal,* Vol. 23, No. 9, 1985, pp. 1418–1423.

[27]Bell, J. H., and Mehta, R. D., "Development of a Two-Stream Mixing Layer from Tripped and Untripped Boundary Layers," AIAA Paper 90-0505, Jan. 1990.

[28]Clemens, N. T., "An Experimental Investigation of Scalar Mixing in Supersonic Turbulent Shear Layers," Ph.D. Dissertation, Mechanical Engineering Dept., Stanford Univ., Stanford, CA, 1991.

[29]Bernal, L. P., and Roshko, A., "Streamwise Vortex Structure in Plane Mixing Layers," *Journal of Fluid Mechanics,* Vol. 170, 1986, pp. 499–525.

[30]Sandham, N. D., and Reynolds, W. C., "Growth of Oblique Waves in the Mixing Layer at High Mach Number," *Seventh Symposium on Turbulent Shear Flows,* Stanford Univ., Stanford, CA, Aug. 1989.

[31]Breidenthal, R., "The Sonic Eddy—A Model for Compressible Turbulence," AIAA Paper 90-0495, Jan. 1990.